

Article

# Study on Aerodynamic Design of the Front Auxiliary Inlet

Junyao Zhang, Hao Zhan and Baigang Mi \*

School of Aeronautics, Northwestern Polytechnical University, Xi'an 710072, China;  
zhangjunyao95@mail.nwpu.edu.cn (J.Z.); zhanhao@nwpu.edu.cn (H.Z.)

\* Correspondence: mibaigang@163.com

**Abstract:** Submerged inlets have been widely used in advanced aircraft due to their excellent stealth characteristics, but they also suffer from poor aerodynamic performance. To improve the aerodynamic efficiency while maintaining stealth capabilities, this paper proposes a design scheme for a front auxiliary inlet with an inlet grille. The front auxiliary inlet is connected to the main inlet to form a composite inlet system. The low-energy upstream airflow that accumulates at the inlet is guided by the front auxiliary inlet to flow into the mainstream, resulting in a stable and high-quality airflow. A certain type of cruise missile was used as the research subject, and intake systems with and without front auxiliary inlets were constructed to compare the inlet performance of the two configurations using the CFD method. Additionally, a sensitivity analysis of the main design parameters of the front auxiliary inlet was carried out. The study reveals that a reasonable design of the front auxiliary inlet can prevent low-energy airflow, which accumulates on the missile body surface, from directly entering the inlet. Moreover, the front auxiliary inlet can inject additional mechanical energy into the low-energy airflow, inhibit airflow separation, and improve the uniformity of the flow field. Under cruise conditions, the total pressure recovery coefficient of the front auxiliary inlet configuration increased by 12.39% compared to the model without a front auxiliary inlet configuration. Furthermore, the total pressure distortion index was reduced by 47.24%.

**Keywords:** submerged inlet; front auxiliary inlet; electromagnetic shielding grille; total pressure recovery coefficient; total pressure distortion index



**Citation:** Zhang, J.; Zhan, H.; Mi, B. Study on Aerodynamic Design of the Front Auxiliary Inlet. *Aerospace* **2023**, *10*, 700. <https://doi.org/10.3390/aerospace10080700>

Academic Editor:  
Konstantinos Kontis

Received: 26 June 2023  
Revised: 2 August 2023  
Accepted: 7 August 2023  
Published: 9 August 2023



**Copyright:** © 2023 by the authors. Licensee MDPI, Basel, Switzerland. This article is an open access article distributed under the terms and conditions of the Creative Commons Attribution (CC BY) license (<https://creativecommons.org/licenses/by/4.0/>).

## 1. Introduction

In future wars dominated by beyond-visual-range warfare, the stealth performance of aircraft will be critical [1]. Relevant research indicates that the inlet and lip account for approximately 40% of the radar wave intensity scattering source within a 30° range in front of the fighter [2–4]. Therefore, to enhance aircraft survivability, stealth design of the inlet must be included in addition to body stealth. For this reason, it is proposed to integrate an electromagnetic grille shield with a submerged inlet. The design of a submerged inlet, integrated into the missile body, has several advantages compared to traditional inlets, including reduced wind resistance and a decrease in the radar scattering area, thereby enhancing aircraft survivability [5,6]. However, the submerged inlet cannot make full use of the incoming flow stamping, leading to increased low-energy airflows entering the pipeline. This results in a suboptimal total pressure recovery coefficient and increased total pressure distortion for the submerged inlet. The integration of an electromagnetic grille shield would exacerbate these issues further.

As early as 1945, Frick et al. designed a NACA submerged inlet and conducted extensive experiments on it. The submerged inlet uses a long, inclined plate with a small inclination angle (about 7°) to introduce airflow into the inlet; however, the inlet's small air intake and low total pressure recovery coefficient make it difficult for it to meet the main inlet requirements [7–12]. Subsequent work by Sun et al. studied the performance of the submerged inlet at high and low speeds with sideslip and positive and negative angles of attack. The surface parameters of the inlet were compared and studied. The results show

that the side edge of the submerged inlet determines the strength of the entrainment vortex, the flow angle of the front lip determines the lateral pressure gradient of the inlet section, and the characteristic parameters of the rear lip profile adjust the distribution of the total pressure and the high- and low-pressure areas at the outlet of the inlet [13].

In an effort to quantify the influence of the low-energy airflow in the boundary layer of the submerged inlet on intake performance, Xie et al. designed a submerged inlet splitter and used wind tunnel and numerical simulation methods to investigate. The results indicate that the total pressure recovery coefficient of the submerged inlet increased by 3.3% after the low-energy airflow was discharged by the shunt, and the circumferential distortion index decreased by 28.2% [14]. Despite the efforts of researchers from several countries, submerged inlets still have some shortcomings, such as low total pressure recovery coefficients and high distortion rates [15–19]. Consequently, researchers have shifted their research focus from inlet design to inlet flow control.

Flow control technology can be categorized into active flow control, passive flow control, and hybrid flow control, based on the need to inject additional momentum or energy [20–29]. Passive flow control technology includes blade vortex generators, convex ridge vortex generators, and others. Among these, blade vortex generators are the most widely used. Jirasek installed two groups of 64 micro-blade vortex generators on the UAV inlet to study the influence of the height of the blade vortex generator on the control effect through wind tunnel experiments. The results indicate that the control effect is optimal when the height is approximately 50% of the local boundary layer thickness, resulting in a 2% increase in the total pressure recovery coefficient of the inlet and a nearly 50% decrease in the distortion index [30]. Vane-type vortex generators are small in size and are often proportional to the thickness of the local boundary layer. Blade-type vortex generators generate a single small streamwise vortex, making blade-type vortex generator arrays a common means for achieving flow control. Gissen et al. studied a vortex generator array through the DOE method and established mapping between the array parameters and inlet performance parameters via the response surface method. The results indicate that control effects are best when the blade height is approximately 30% of the boundary layer thickness and the relative flow direction deflection of the blade is  $13^\circ$  [31]. To prevent the boundary layer on the surface of the missile body from entering the inlet, Saheby et al. arranged a convex ridge vortex generator in the inlet and studied the structure of the vortex and boundary layer transition by numerical simulation. The results show that the convex ridge vortex generator can significantly improve the efficiency of the inlet in subsonic flight; however, since the convex ridge vortex generator is situated on the surface of the missile body, it is sensitive to the angle of the airflow passing through the convex ridge, reducing the flow control efficiency significantly at large sideslip angles [32]. Sun et al. designed a bumped vortex generator for the submerged inlet and verified it through wind tunnel experiments. The results indicate that the upstream missile body's boundary layer is effectively pushed away from the inlet entrance using the bubbling vortex generator. This improves the inlet flow quality and performance of the submerged inlet. At a free-flow Mach number of 0.73, the total pressure recovery coefficient of the submerged inlet can be increased by 3.7% [33,34].

Active flow control technology includes jet vortex generators, boundary layer blowing and suction, and more. Neal et al. conducted a comparative analysis of the layout forms of micro-jets, including the circumferential layout, the axial layout of the bottom plate, the V-shaped layout of the bottom plate, and other schemes. The results indicate that all micro-jets layouts effectively reduce the distortion index of the inlet; however, the circumferential and V-shaped angle of about  $80^\circ$  performs better in terms of the control effect [35]. Yadav et al. studied the Y-shaped double inlet and compared the effect of a slotted synthetic jet and a row of four circular synthetic jets on improving the aerodynamic performance of the aircraft inlet. The slotted synthetic jet has greater control force because the vortex generated by the slotted synthetic jet is distributed along the spanwise direction, making the ejected airflow's mass and vorticity easier to mix with the mainstream [36]. Cheng

et al. proposed a submerged inlet flow field control scheme based on surface blowing and suction of the missile body. CFD numerical simulation was used to explore the influence of this flow control scheme on the inlet's performance. The research results indicate that the control scheme based on the surface blowing and suction of the missile body improves the intake performance to a certain extent, but requires additional airflow sources. Usually, high-pressure airflow is extracted from the compressor directly, meaning the blowing flow rate cannot be too high; otherwise, it will impact the engine performance [37,38].

While both active and passive flow control technologies can improve the intake performance of submerged inlets to a certain extent, each approach has limitations. While passive flow control does not require additional energy, its effectiveness can be limited in some flight conditions. Meanwhile, active flow control strategies can adapt flexibly to changing flight conditions, but additional energy injection is required. A novel method that differs from conventional active and passive flow control is proposed in this paper. To address the shortcomings of the low total pressure recovery coefficient and high total pressure distortion indices of submerged inlets with grilles, a front auxiliary inlet was creatively designed. The feasibility of the scheme was verified using CFD numerical simulation technology, followed by an exploration of the influence of the relevant parameters of the front auxiliary inlet on intake performance. Sensitivity analyses of the related parameters are provided.

## 2. Front Auxiliary Inlet Design

While the stealth characteristics of submerged inlets are generally favorable, their larger cavity structures still exhibit discernible electromagnetic reflection characteristics [1]. Electromagnetic grille shielding technology can help scatter the electromagnetic wave in the grille, reflecting most of the energy of the incident electromagnetic wave in a direction undetectable by radar. It can also force the electromagnetic wave entering the inlet to reflect multiple times between the grille and the cavity, reducing the energy of the electromagnetic wave and increasing its scattering degree in the cavity, thereby further reducing the intensity of the echo. Given the modern aircraft's prioritization of stealth performance and the importance of this feature, greater emphasis is placed on stealth design during the design process; therefore, the application of electromagnetic grille shielding technology to submerged inlets was considered.

### 2.1. Electromagnetic Shielding Grille Design

The main design parameters of electromagnetic shielding grille include the grille diversion angle ( $i$ ), grille thickness ( $t$ ), grille hole profile shape, grille hole characteristic length ( $d$ ), adjacent grille hole spacing ( $s$ ), porosity ( $p$ ), and more, as shown in Figure 1. Electromagnetic grille shielding technology is a mature stealth technology and has been widely verified in many advanced aircraft designs. Table 1 provides the design parameters directly; therefore, we will not discuss the design process further.

**Table 1.** Main parameters of grille.

Parameter	Values
Grille diversion angle	25°
Grille thickness	2.2 mm
Grille hole profile shape	square
Grille hole characteristic length	5.3 mm
Adjacent grille hole spacing	1 mm
Porosity	70%

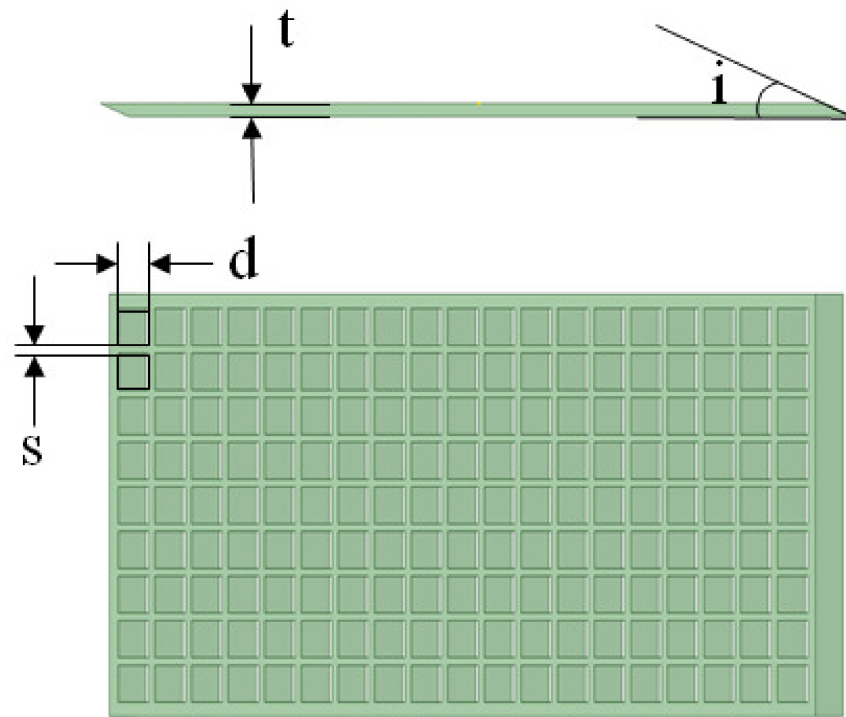


**Figure 1.** The main parameters of the grille's schematic diagram.

## 2.2. Flow Characteristics of Submerged Inlet

To improve the intake efficiency of the submerged inlet, it is essential to understand the intake mechanism. The submerged inlet primarily relies on the pressure gradient perpendicular to the incoming flow direction at the front lip and the entrainment vortex generated by the side edge to drive the external airflow into the inlet (Figure 2). The main factor affecting the inlet's performance is that the entrance of inlet on the body surface is located in the boundary layer near the missile body. As a result, low-energy airflow inevitably flows into the inlet, inducing large-scale separation vortices and large inlet outlet total pressure distortion [39] (Figure 3).

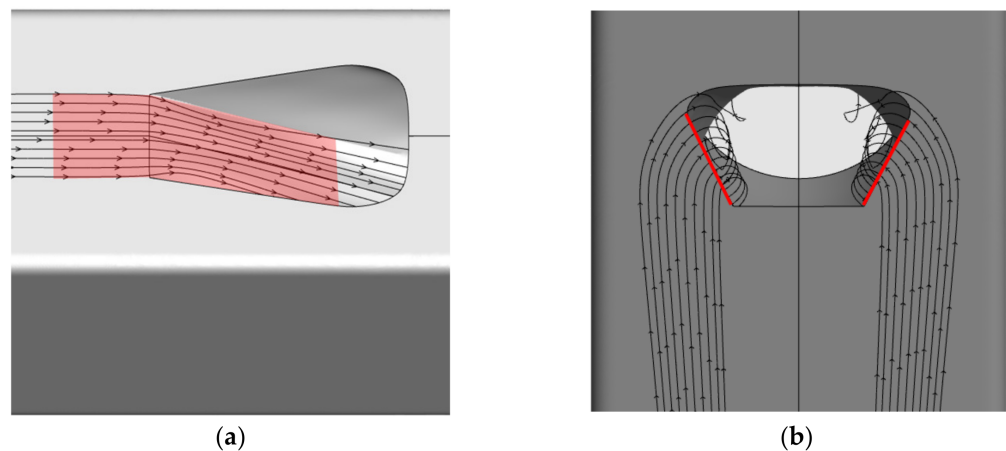


**Figure 2.** Intake mechanism of submerged inlet. (a) Pressure gradient at lip; (b) vortex generated by side edges.

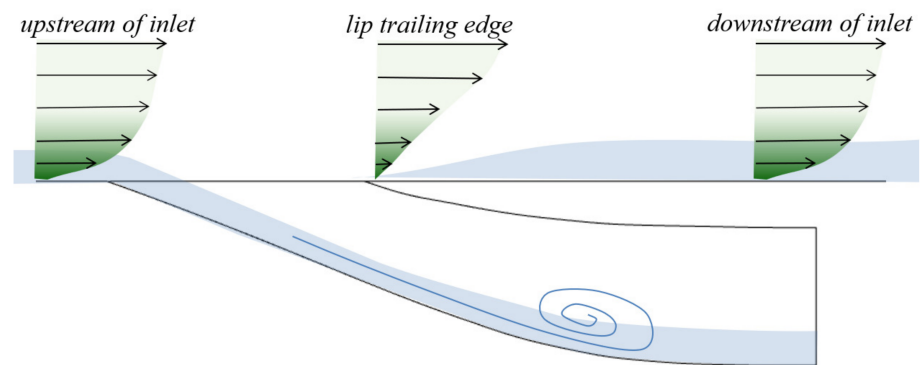


**Figure 3.** Flow characteristics diagram of submerged inlet.

When the submerged inlet is covered with a grille, the effective area of the inlet opening is first reduced. Secondly, the inlet can no longer rely on the pressure gradient perpendicular to the incoming flow direction at the front lip and the entrainment vortex generated by the side edge to drive the external airflow into the inlet. Finally, when the airflow flows into the grille hole, it shrinks and its velocity increases. Upon exiting the grille, the airflow expands and the velocity decreases. This inflow and outflow process results in “impact loss”, which further reduces the energy of the airflow flowing into the inlet therefore, efficient flow control methods are necessary when combining electromagnetic grille shielding technology with the submerged inlet.

### 2.3. Design Idea of Front Auxiliary Inlet

The limited space for arranging the inlet in an aircraft is constrained by the internal structure, making it crucial to maximize the intake efficiency. This can be achieved by (1) reducing or eliminating the influence of low-energy airflow in the missile body boundary layer near the inlet entrance and (2) improving the mechanical energy of the airflow into the inlet and organizing the directional migration of the low-energy fluid in the inlet to avoid the large-scale separation vortex generated by the large accumulation of low-energy airflow. To address this, a submerged inlet configuration with a front auxiliary inlet was designed, as shown in Figure 4. A submerged inlet with a grille is arranged upstream of the main inlet’s entrance, which is referred to as the front auxiliary inlet. The front auxiliary inlet is designed according to the submerged inlet design method, and the designed front auxiliary inlet and main inlet are pruned and smoothed at their intersection line. In Figure 4, the gray part represents the portion that needs to be retained after the inlet’s trim, while the yellow part denotes the portion that requires deletion after the trim.

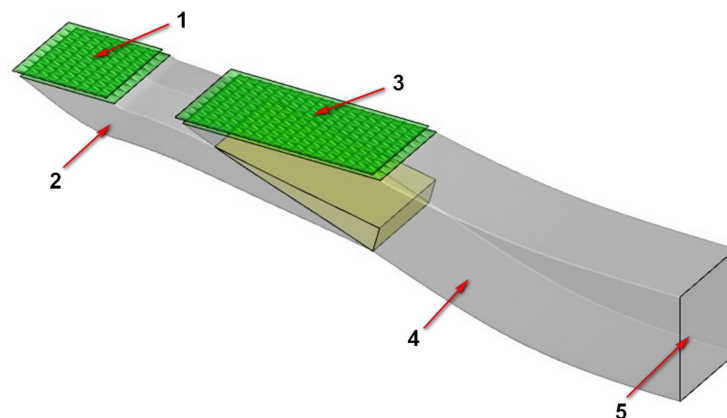


**Figure 4.** Submerged inlet configuration with front auxiliary inlet. Number 1 is the electromagnetic shielding grille at the entrance of the front auxiliary inlet; 2 is the front auxiliary inlet; 3 is the electromagnetic shielding grille at the entrance of the main inlet; 4 is the main inlet; and 5 is the outlet.

Figure 5 shows the flow mechanism of the front auxiliary inlet configuration. The front auxiliary inlet is connected to the main inlet and serves to introduce a large amount of low-energy airflow, which accumulates on the body surface, into the front auxiliary inlet. This avoids the low-energy airflow directly flowing into the main inlet and disrupting the uniformity of the inlet's internal flow field. The front auxiliary inlet and the main inlet form a device similar to an ejector, which uses a high-speed and high-energy flow to eject another low-speed and low-energy flow. The low-speed airflow brought in by the front auxiliary inlet and the high-speed airflow brought in by the main inlet mix appropriately and merge at the intersection. This allows for energy transfer between the airflows with different velocities and delays the separation of airflow near the wall. Finally, this achieves the objective of improving the total pressure recovery coefficient and reducing distortion.

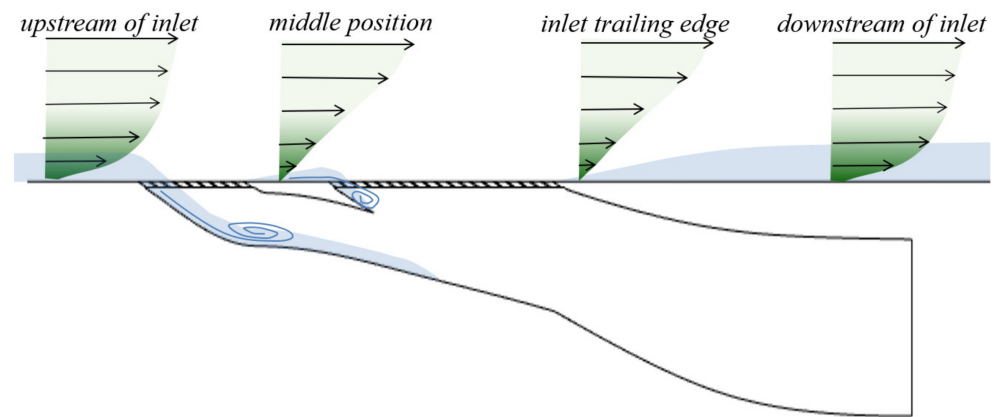


Figure 5. Flow characteristics of front auxiliary inlet configuration.

#### 2.4. Parameter Optimization of Front Auxiliary Inlet

Parameter optimization, as a mature technology, has been widely used in designing advanced aircraft. This section presents the construction process of the optimization model and its results, but does not delve into the optimization algorithm's details. The design parameters of the front auxiliary inlet, as shown in Figure 6, primarily include the diversion angle  $\theta$ ; the entrance area  $S_{front,open}$ ; the throat area  $S_{front,throat}$ , which is the cross-sectional area of the front auxiliary inlet at A–A in the figure; the exit area  $S_{front,outlet}$ , which is the cross-sectional area of the front auxiliary inlet at B–B in the figure; the area expansion ratio  $k$ , which is the ratio of the outlet area of the front auxiliary inlet to the throat area; the distance between the rear lip of the front auxiliary inlet and the front lip of the main inlet  $L_1$ ; and centerline offset of the front auxiliary inlet  $L_2$ .

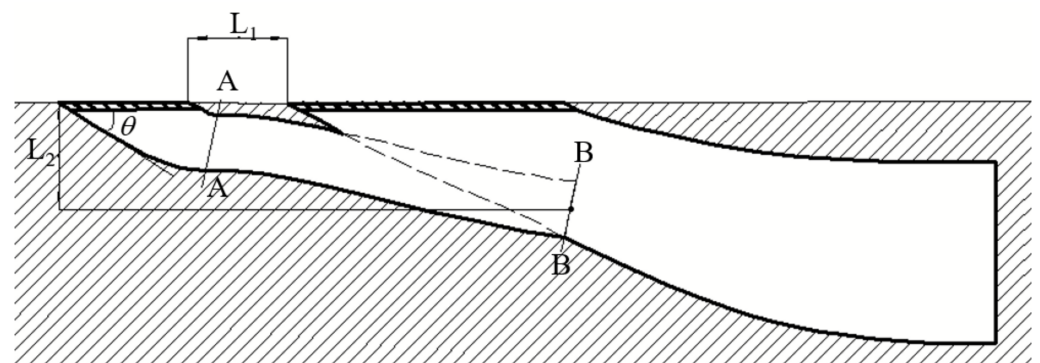


Figure 6. The schematic diagram of the main design parameters of the front auxiliary inlet.

The parameters of the front auxiliary inlet configuration are optimized based on the particle swarm optimization (PSO) algorithm. Firstly, based on the existing inlet design

experience, the preliminary design parameters of the front auxiliary inlet are given. Next, the configuration is parameterized based on the initial design, simplifying optimization of the original geometric model of the front auxiliary inlet into the optimization of its design parameters. It should be noted that since the inlet entrance is covered with a grille, the spanwise length was kept unchanged throughout the optimization process to maintain the integrity of each grille hole. The opening area of the front auxiliary inlet is controlled by adjusting the number of grille holes along the flow direction.

In the established optimization model, the algorithm parameters are set as follows: the number of iterations is 150; particle number 20; global increment 0.9; particle increment 0.9; inertial factor 0.9; maximum speed 0.1; and the maximum number of failed iterations is 5. The design variables are  $(k, L_1, L_2, n)$ . The optimization goal is to obtain the maximum ratio of the total pressure recovery coefficient to the total pressure distortion index. The formula is as follows:

$$\begin{cases} \sigma = \frac{P_{AIP}}{P_0} \\ D_1 = \frac{P_{AIP,max} - P_{AIP,min}}{P_{AIP,max}} \\ \eta = \frac{\sigma}{D_1} \end{cases} \quad (1)$$

where  $\sigma$  is the total pressure recovery coefficient;  $P_{AIP}$  is the average total pressure (mass-averaged) of the AIP section;  $P_0$  is the total pressure of the incoming flow;  $D_1$  is the total pressure distortion index;  $P_{AIP,max}$  is the maximum total pressure of the AIP section;  $P_{AIP,min}$  is the minimum total pressure of the AIP section; and  $\eta$  is the ratio of the total pressure recovery coefficient to the total pressure distortion index.

The optimization model can be described as follows:

$$\begin{cases} \text{Max } \eta = \frac{\sigma}{D_1} \\ \text{s.t. } 0.2 \leq k \leq 2 \\ 16 \leq L_1 \leq 95 \\ 18 \leq L_2 \leq 40 \\ 6 \leq n \leq 15 \end{cases} \quad (2)$$

The range of design variables and optimization results are shown in Table 2.

**Table 2.** Design variable value range and optimization results.

Design Variable	Value Ranges	Optimal Value
$k$	0.2~2	0.8
$L_1$	16~95 mm	42.5 mm
$L_2$	18~40 mm	40 mm
$n$	6~15	9

### 3. Research Object

The main focus of this paper is to compare the performance of two different inlet configurations. Figure 7a,b respectively show two types of inlet configurations: the submerged inlet configuration without a front auxiliary inlet (referred to as the “without front auxiliary inlet configuration”) and the compound inlet configuration with a front auxiliary inlet (referred to as the “front auxiliary inlet configuration”). The rectangular-shaped missile body has rounded corners, a total length of 1085 mm, and a width of 110 mm. The submerged inlet is located on the lower abdomen plane of the missile body, with the grille highlighted in green. In order to facilitate the observation, the upper and lower surfaces of the missile body are inverted in subsequent related pictures and only displayed in half-mode. The main parameters of the front auxiliary inlet and the main inlet are listed in Tables 3 and 4, respectively, to provide a clear reference for the comparison and analysis of the performance of the two configurations.

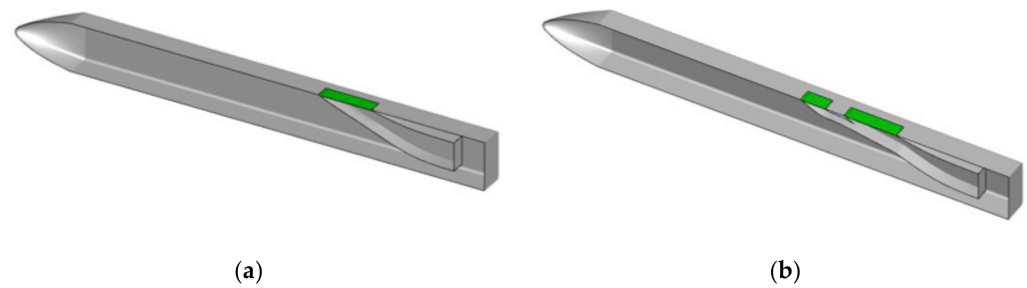


**Figure 7.** Inlet and missile body. (a) The without front auxiliary inlet configuration; (b) the front auxiliary inlet configuration.

**Table 3.** Main design parameters of front auxiliary inlet.

Parameter	Values
Shape of outlet	Rectangle
Shape of entrance	Rectangle
Size of outlet	60.4 mm × 16.1 mm
Size of entrance	60.4 mm × 58.4 mm
Length of inlet	223.8 mm
Center line offset	40 mm
Diversion angle	25°

**Table 4.** Main parameters of main inlet.

Parameter	Values
Shape of outlet	Rectangle
Shape of entrance	Rectangle
Size of outlet	65 mm × 65 mm
Size of entrance	122.9 mm × 60.4 mm
Length of inlet	313.6 mm
Center line offset	53.8 mm

## 4. Method of Calculation

### 4.1. Governing Equation

The three-dimensional numerical simulation was performed using FLUENT software, which utilizes the Navier–Stokes equations solved based on the finite volume method. The second-order upwind scheme is applied to the flow direction, the central difference is used for the diffusion term, and the coupled method is employed for the pressure-velocity coupling. In this paper, the Spalart–Allmaras turbulence model is mainly applied in the numerical simulation. This turbulence model is a single equation model that is capable of directly solving the modified turbulent viscosity. It is widely used in the aviation field due to its high accuracy and relatively low computational cost. Due to the accurate simulation of the flow details, such as the boundary layer transition, turbulence separation, turbulence intensity, etc., the Spalart–Allmaras turbulence model is an ideal choice for many flow scenarios in this study [27].

### 4.2. Calculation Grid and Calculation Settings

In the absence of sideslip, even though the half-mode approach reduces the computational grid count, its reliance on symmetric boundary conditions guides the flow in a constrained manner, thus preventing the formation of a comprehensive three-dimensional flow structure within the intake duct. To address this limitation, this study adopted the full-mode approach for the calculations. Unstructured polyhedral grids are used to simulate the flow field in both the without front auxiliary inlet and front auxiliary inlet configurations. The far-field computational domains of the two configurations are the same, and they

are both cuboids with the following dimensions: length, 21 m; width, 5.3 m; and height, 5.3 m, as illustrated in Figure 8. The unstructured polyhedral grids enable the simulation to accurately capture the complex flow features associated with the inlet configurations and are capable of identifying areas of potential flow separation.

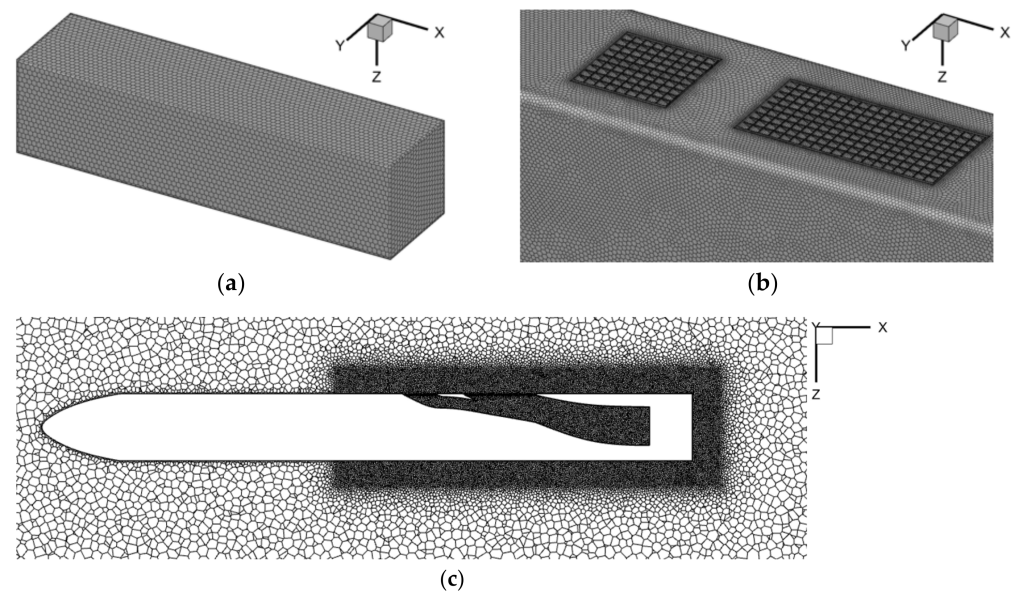


**Figure 8.** Computational grid. (a) Computational domain grid; (b) local grid at the grille; (c) grid at a symmetrical cross-section.

The grid size of the two inlet configurations was set to be the same to ensure a fair comparison. To accurately capture the complex flow features on the surface of the missile and inlet, the enhanced wall treatment (EWT) technique was employed in this study. This technique requires a very dense near-wall grid with  $y^+$  close to 1; however, an excessively dense boundary layer grid can lead to low grid quality and reduce the accuracy of the calculations. Therefore, the boundary layer grid was properly adjusted to maintain the accuracy of the simulation. The final number of boundary layers was set to 10, with the first layer of grid height being 0.01 mm and a growth rate of 1.2. The without front auxiliary inlet configuration has approximately 3.0 million grids, while the front auxiliary inlet configuration has approximately 3.6 million grids. These grid sizes are considered sufficient to accurately capture the flow features and turbulence characteristics of the two configurations. The use of the same grid sizes for the two configurations ensures a reliable comparison of their performance.

The boundary conditions for the numerical simulation were set according to Figure 9. The far field of the computational domain was subjected to the pressure far field boundary condition, and the free flow parameters were assigned based on the atmospheric conditions at an altitude of 5 km, with  $M_0 = 0.7$ ,  $\beta = 0$ , and  $\alpha = 2^\circ$ . The outlet was assigned the pressure outlet boundary condition, and the pressure was set to the corresponding pressure for  $M_e = 0.4$ . The surfaces of the missile body, inlet, and grille were set to non-slip adiabatic wall boundary conditions, which simulate the no-slip effect of the air near the wall and ensure that there is no heat transfer between the fluid and the solid surfaces. These boundary conditions are considered appropriate for the numerical simulation and were used consistently across both the without front auxiliary inlet and front auxiliary inlet configurations.

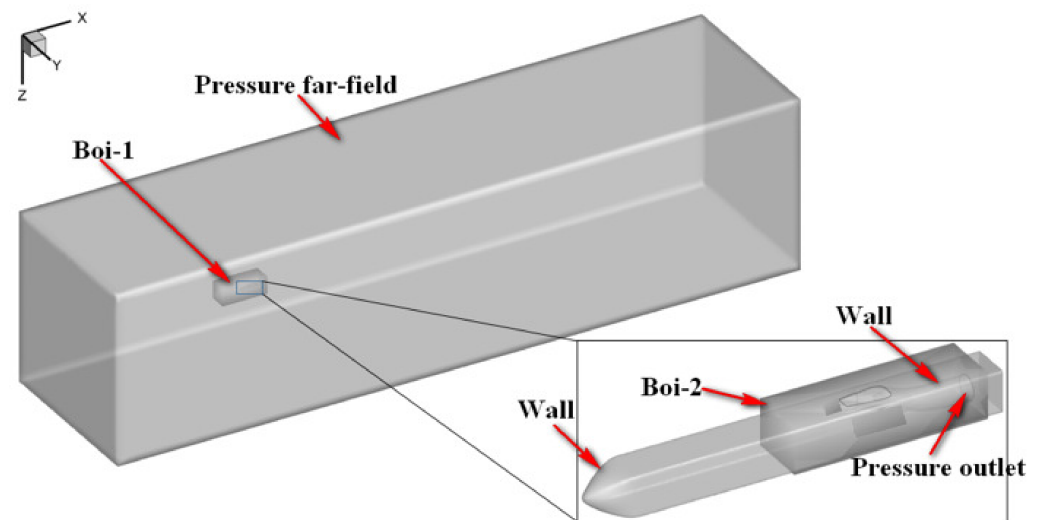


**Figure 9.** Setting of boundary conditions.

#### 4.3. Grid Independence Analysis

In order to determine the appropriate grid size for the flow field simulation, a grid independence analysis was conducted for the without front auxiliary inlet configuration. To minimize the impact of the number of grid nodes on the accuracy of the simulation results, four grid configurations were generated by adjusting the grid density of the object surface. The number of body grids for the four configurations were 1.4 million, 3.0 million, 7.0 million, and 10 million, respectively. The simulation results for the four grid configurations are presented in Table 5. Using the results obtained from the 10 million grid configuration as the reference, the error of the 1.4 million grid configuration is relatively large, at approximately 1.9%. The errors for the 3.0 million and 7.0 million grid configurations are both less than 0.5%, which meets the required level of accuracy. To balance computational efficiency and accuracy, this study used the grid configuration with 3.0 million grid nodes for all the simulations.

**Table 5.** Grid scheme.

Grid Scheme	Number of Grids (Millions)	$\sigma$	Error
1	1.4	0.7756	0.01958
2	3.0	0.7638	0.00407
3	7.0	0.7629	0.00289
4	10.0	0.7607	/

#### 4.4. Example Verification

The centerline variation of the main inlet in this study is consistent with that in Reference [35]. The main difference is that the inlet considered in this study was designed for stealth performance and is covered by a grille at the inlet. Consequently, the shape of the inlet profile was modified to accommodate the grille. Specifically, the shape of the opening on the surface of the missile body was changed from the original trapezoid with rounded corners to a rectangle. To validate the accuracy of the numerical simulation method used in this study, the flow field around the missile body and the submerged inlet described in Reference [35] was simulated and compared to the relevant experimental data. The submerged inlet described in Reference [35] is shown in Figure 10.

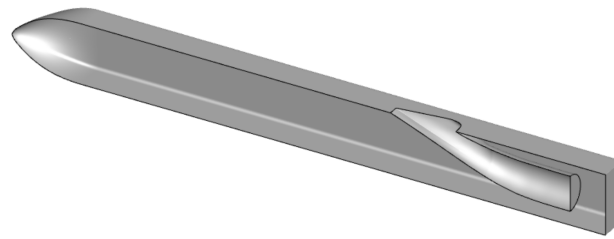


**Figure 10.** Submerged inlet in reference [35].

The numerical study results indicate that under the conditions of  $M_0 = 0.73$ ,  $M_e = 0.4$ , and an altitude of 5000 m, the average total pressure recovery coefficient at the outlet section was 92.20%. In this study, under the same conditions, the average total pressure recovery coefficient at the outlet section was 92.44%, with a numerical simulation error of only 0.26%. Figure 11 shows the distribution of total pressure at the outlet section, which matches the experimental results very well; therefore, the numerical simulation method used in this study, which couples the internal and external flow fields, is considered accurate and reliable, and is suitable for the comprehensive analysis of the missile/inlet configuration.

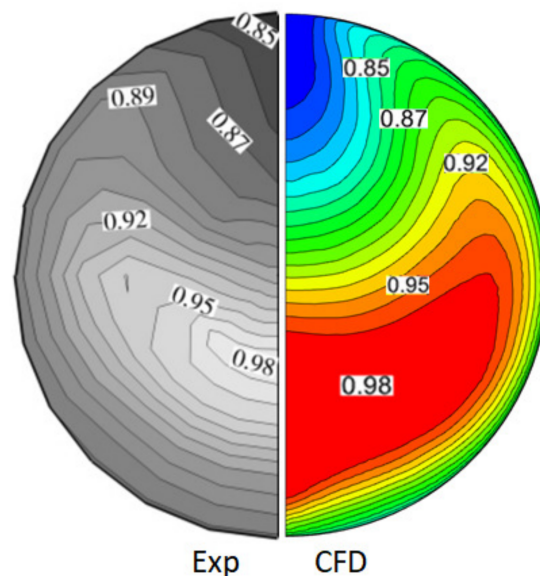


**Figure 11.** Total pressure distribution at AIP.

## 5. Results and Analysis

This section investigates the impact of the front auxiliary inlet on the inlet performance, with a focus on the boundary layer development, total pressure distribution, Mach number distribution, and streamwise vortex development. Both cases where the inlet was equipped with and without the front auxiliary inlet are examined. Additionally, a study on the adaptability of the front auxiliary inlet under off-design conditions was conducted.

### 5.1. Boundary Layer Development Upstream of Inlet

As shown in Figure 12, there are seven monitoring surfaces arranged in the direction of airflow on the missile body surface. Each monitoring surface measures 101 mm in width and 11 mm in height. The x-coordinates of the monitoring surfaces are 0.128 m, 0.195 m, 0.297 m, 0.397 m, 0.498 m, 0.599 m, and 0.701 m, respectively. The sixth monitoring surface is aligned with the leading edge of the opening of the front auxiliary inlet on the missile body surface, while the seventh monitoring surface is aligned with the leading edge of the opening of the inlet on the missile body surface.

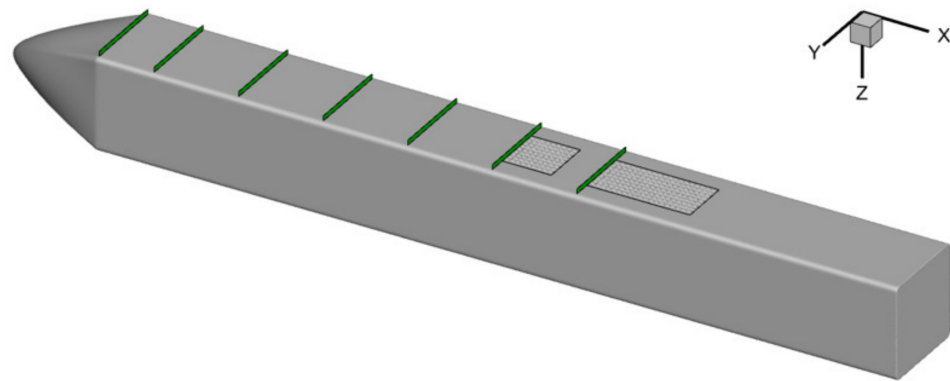


**Figure 12.** Monitoring surface of missile body.

Figure 13 illustrates the distribution of the total pressure recovery coefficient on the monitoring surfaces. Due to the high level of symmetry, a half-model representation is used. The left side represents the without front auxiliary inlet configuration, while the right side represents the front auxiliary inlet configuration. The dashed line in the middle indicates the position of the symmetry plane. As observed, the low-energy airflow accumulates gradually along the flow direction, leading to an increase in the boundary layer thickness. After the  $x = 0.297$  m position, the boundary layer thickness reaches a steady state due to the effect of the friction force acting on the missile body surface. The total pressure distribution before  $x = 0.599$  m remained consistent with and without the front auxiliary inlet.

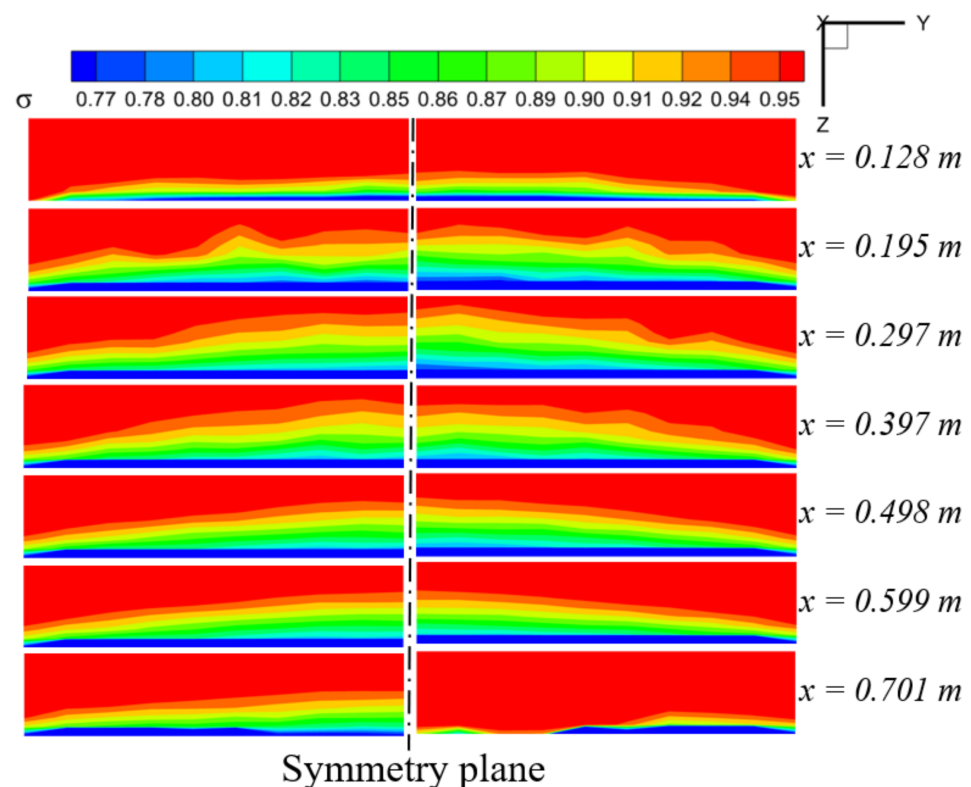


**Figure 13.** Distribution of total pressure recovery coefficient on monitoring surface (the left side is the without front auxiliary inlet configuration, and the right side is the front auxiliary inlet configuration).

At the  $x = 0.701$  m position, the thickness of the boundary layer of the front auxiliary inlet configuration significantly decreased near the symmetry plane, which is one-fifth of that observed in the without front auxiliary configuration. This is because the low-energy

airflow near the symmetry plane flows into the front auxiliary inlet; however, the length from the trailing edge of the front auxiliary inlet to the leading edge of the main inlet is limited and, as a result, the boundary layer is still in the initial stage of accumulation and has not yet formed at a larger scale.

## 5.2. Total Pressure Recovery Coefficient Distribution

### 5.2.1. The Distribution of Total Pressure Recovery Coefficient on the Symmetry Plane

The distribution of the pressure recovery coefficient on the symmetry plane is shown in Figure 14. The airflow with lower total pressure in the boundary layer of the without front auxiliary inlet configuration flows directly into the inlet from the front edge of the inlet and forms an obvious low-pressure area on the side with a larger radius of curvature.

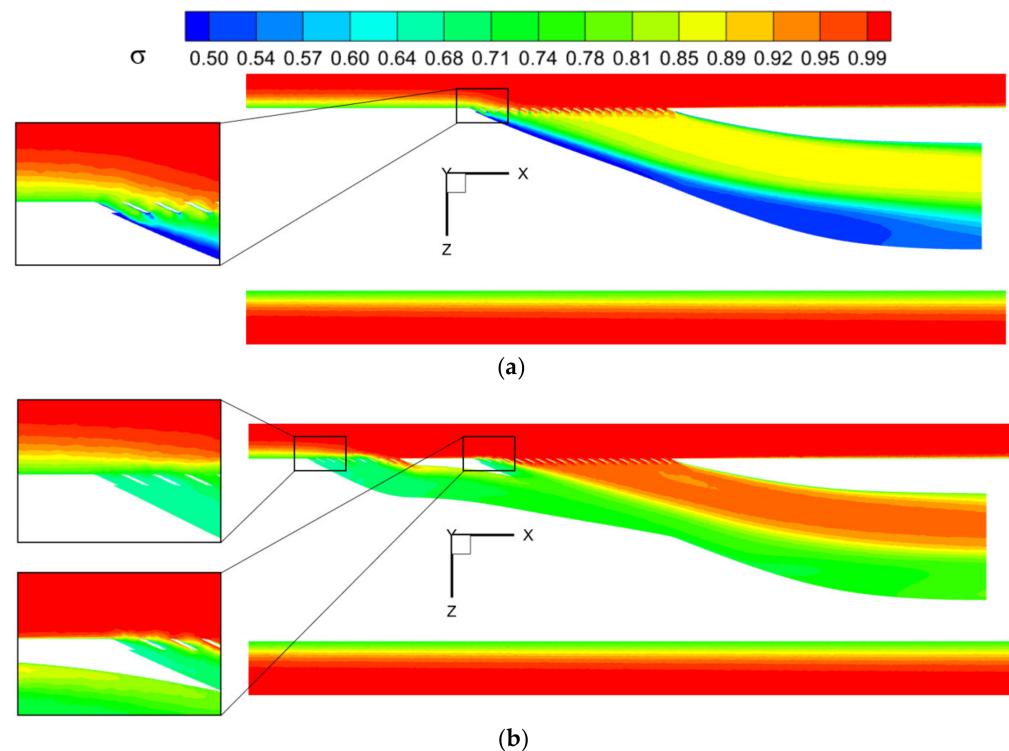
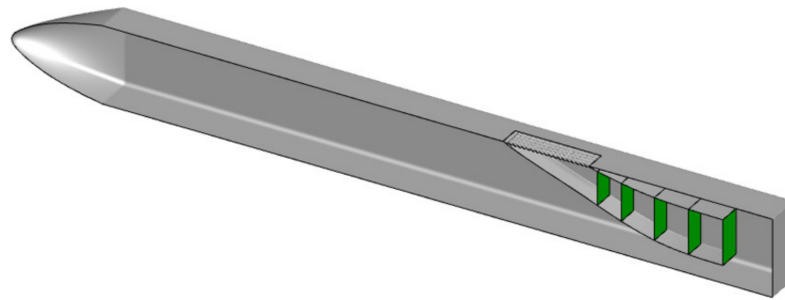


**Figure 14.** The distribution of total pressure recovery coefficient on the symmetry plane. (a) The without front auxiliary inlet configuration; (b) the front auxiliary inlet configuration.

For the front auxiliary inlet configuration, the low-energy flow in the boundary layer mainly flows into the front auxiliary inlet from the front edge of the front auxiliary inlet. The low-energy flow into the main inlet is significantly less than the without front auxiliary inlet configuration. The thickness of the boundary layer at the front lip of the main inlet is about one-fifth of that of the without front auxiliary inlet configuration, and there is no obvious low-pressure area on the side of the inlet with a larger internal curvature radius. The total pressure recovery coefficient inside the inlet is significantly higher than that of the without front auxiliary inlet configuration.

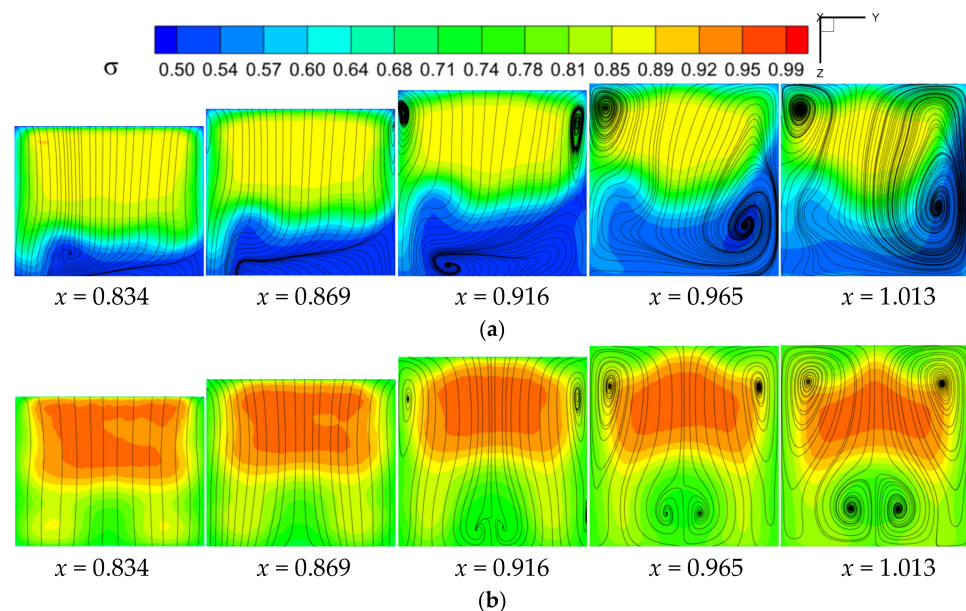
### 5.2.2. The Distribution of Total Pressure Recovery Coefficient along the Flow Direction

Five monitoring surfaces are arranged inside the inlet in the direction of airflow, as depicted in Figure 15. The x-coordinates of the monitoring surfaces are 0.834 m, 0.869 m, 0.916 m, 0.965 m, and 1.013 m, respectively. The fifth monitoring surface is located at the inlet exit.



**Figure 15.** Monitoring surface inside the inlet (display with a half-model).

The total pressure recovery coefficient distribution with streamlines at the monitoring surface of the without front auxiliary inlet configuration is shown in Figure 16a. After the low-energy airflow flows into the inlet, the obvious separation vortex is formed on the side of the larger curvature radius of the inlet. The low-energy airflow at  $x = 0.834$  m only accounts for one-fifth of the monitoring surface area. With the further development of the airflow in the inlet, the area of the low-energy airflow gradually increases due to the friction of the inlet wall and the mixing between different velocity airflows. After  $x = 0.916$  m, the low-energy airflow accounts for more than a third of the monitoring area. It can be seen from the streamline diagram that the separation vortex at  $x = 0.869$  m only appears at the low-energy airflow on the side of the larger curvature radius of the inlet. With the flow of the airflow, the friction on the wall of the inlet continues to consume the energy of the airflow. At  $x = 0.916$  m, a pair of separation vortices is also generated on the side with a smaller radius of curvature of the inlet, closer to the wall. As the flow's energy further dissipates, at  $x = 0.965$  m, the separation vortex in the upper right corner merges with the bottom separation vortex, forming a larger-scale separation vortex. The scale of the merged separation vortex further expands at  $x = 1.013$  m.



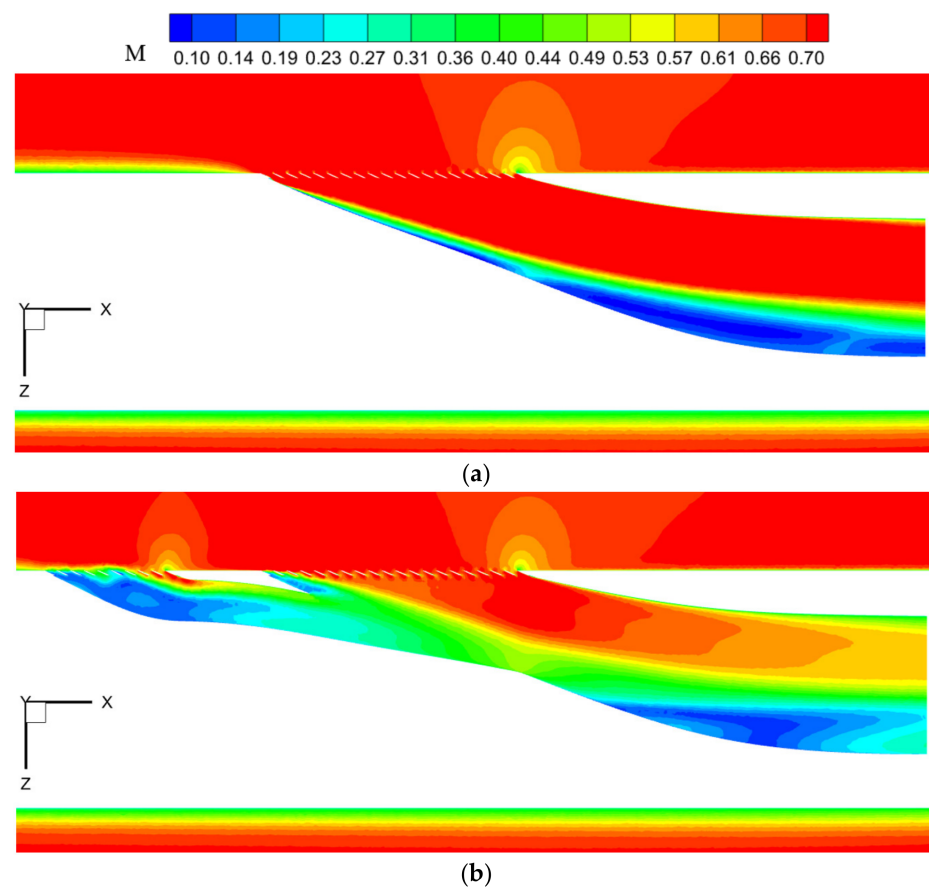
**Figure 16.** The distribution of total pressure recovery coefficient with streamlines. (a) The without front auxiliary inlet configuration; (b) the front auxiliary inlet configuration.

Figure 16b displays the distribution of the total pressure recovery coefficient with streamlines in the monitoring surface of the front auxiliary inlet configuration. At  $x = 0.834$  m and  $x = 0.869$  m, the airflow is relatively uniform, and there is no evident separation phenomenon. This is due to the fact that the majority of low-energy airflow flows into the front auxiliary inlet, resulting in higher airflow energy in the main inlet

and a more uniform flow field, thus improving its ability to resist separation. As the flow develops, at  $x = 0.916$  m, it is influenced by the friction of the inlet wall and the pressure gradient, leading to the formation of a pair of separation vortices near the wall on the side of the inlet with a smaller radius of curvature. Additionally, a pair of separation vortices also form at the middle position on the side of the inlet with a larger radius of curvature. These separation vortices gradually increase in size at  $x = 0.916$  m and  $x = 1.013$  m. By comparing Figure 16a,b, it is apparent that the configuration with the front auxiliary inlet has a significantly higher total pressure recovery coefficient and a stronger resistance to separation compared to the configuration without the front auxiliary inlet.

### 5.3. Mach Number Distribution

Figure 17 displays the distribution of the Mach number on the symmetry plane. In Figure 17a, it is evident that stratification exists between the high- and low-speed airflows. The airflow velocity on the side with a larger radius of curvature is significantly lower than that on the side with a smaller radius of curvature. As the airflow develops within the inlet, the low-energy airflow near the wall boundary layer and the airflow away from the boundary layer interfere with one another. The low-energy airflow exerts a significant “drag” effect on the high-energy airflow and fast flow rate, while the fast-flowing, high-energy airflow rolls the low-energy airflow with a slow flow rate from the wall position to the center of the inlet. Finally, an evident separation vortex forms on the side with a larger radius of curvature, contributing to strong mixing loss.



**Figure 17.** The Mach number distribution cloud chart with streamline on the symmetry plane. (a) The without front auxiliary inlet configuration; (b) the front auxiliary inlet configuration.

In Figure 17b, a large amount of low-energy boundary layer airflow enters the front auxiliary inlet, resulting in noticeable separation phenomena within the duct. A small amount of low-energy airflow from the boundary layer enters the main inlet, causing

slight separation near the leading edge of the duct; however, as the flow progresses, these separation vortices are inhibited. Furthermore, comparing Figure 17a with Figure 17b, it is evident that the configuration with the front auxiliary inlet better accomplishes the task of decelerating and pressurizing the incoming flow, while also providing a more uniform internal flow field.

#### 5.4. Development of Streamwise Vortices

To conduct a more detailed and comprehensive study on the formation and evolution process of vortices inside the intake duct, the computational domain inside the duct is divided into left and right sections at the symmetry plane, and each section is presented separately. Figure 18 shows the iso-surface of vortices. The most widely used Q-criterion was chosen as the method to identify the vortices, and the iso-surface is colored based on the Mach number.

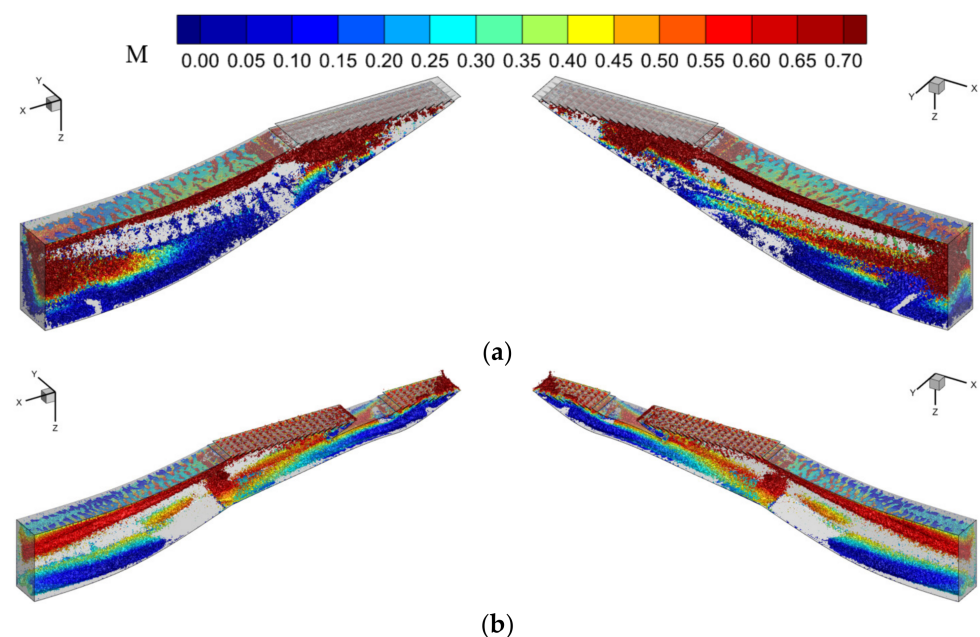


**Figure 18.** Vortical structures developed in air-inlet visualized by  $Q = 0.1$  iso-surfaces. (a) The without front auxiliary inlet configuration; (b) the front auxiliary inlet configuration.

Figure 18a reveals that the streamwise vortices in the without front auxiliary inlet configuration begin to develop from the grille, with the scale increasing along the flow direction, and reach maximum intensity near the outlet. With the low-energy airflow in the boundary layer flowing directly into the inlet, the airflow has a strong mixing phenomenon at different speeds near the inlet exit, forming numerous separation vortices and creating a high degree of inhomogeneity in the flow field.

In Figure 18b, the streamwise vortex in the front auxiliary inlet configuration begins to develop from the grille at the inlet of the front auxiliary inlet. Due to the low-energy airflow in the boundary layer flowing into the front auxiliary inlet, evident airflow separation occurs inside the front auxiliary inlet; however, the separation vortex does not develop along the flow direction and expand the scale, and even the scale of the downstream streamwise vortex at the intersection of the front auxiliary inlet and the main inlet is significantly reduced.

By observing the vorticity diagram on the iso-surface, it can be seen that the front auxiliary inlet and the main inlet form an ejector-like device. Firstly, the low-energy airflow is absorbed by the front auxiliary inlet to ensure that the airflow flowing into the main inlet is of high energy. Then, the high-speed and high-energy flow in the main inlet ejects the low-speed, low-energy flow in the front auxiliary inlet. At the intersection of the front

auxiliary inlet and the main inlet, through the mixing effect, the high-speed and high-energy flow in the main inlet transfers energy to the low-speed and low-energy flow flowing out of the front auxiliary inlet, which suppresses the development of the separation vortex on the side with a larger curvature radius of the inlet. The mixed flow formed by mixing exhibits good uniformity, and there is no evident separation vortex within a specific range downstream of the intersection. With the inlet wall friction, a certain scale of separation vortex is formed near the outlet wall, but this separation vortex's scale is significantly smaller than that of the inlet without a front auxiliary inlet.

### 5.5. Applicability of the Front Auxiliary Inlet under Different Operating Conditions

The total pressure recovery coefficient's size illustrates the extent of flow losses, with a larger value indicating lower flow losses. The total pressure distortion index reflects the level of distortion within the flow field, determined by the difference between the maximum and minimum values of the total pressure across the entire plane. The formulas for calculating the total pressure recovery coefficient ( $\sigma$ ) and the total pressure distortion index ( $D_1$ ) are shown in Formula (1). Table 6 displays the total pressure recovery coefficient and total pressure distortion index at the outlet of the two inlet configurations when  $M_0 = 0.7$ ,  $\beta = 0$ , and  $\alpha = 2^\circ$ . The total pressure recovery coefficient at the outlet of the front auxiliary inlet configuration is 0.8719, with a total pressure distortion index of 0.2041. Compared to the inlet configuration without a front auxiliary inlet, the average total pressure recovery coefficient at the outlet increases by 12.39%, and the total pressure distortion index reduces by 47.24%.

**Table 6.** Performance comparison of two inlet configurations at the outlet.

Parameter	$\sigma$	$D_1$
Without front auxiliary inlet configuration	0.7638	0.3869
Front auxiliary inlet configuration	0.8719	0.2041

Figures 19–21 present a comparison of the inlet performance under different angles of attack, angles of sideslip, and inflow Mach numbers. The results demonstrate that the front auxiliary inlet significantly improves the intake quality within the calculated range. It is noteworthy that its performance advantage is not limited to specific operating conditions but exhibits wide applicability. This implies that the front auxiliary inlet can enhance the inlet performance across various flight conditions. It maintains the uniformity and stability of the incoming airflow, delivering higher-quality air to the engine, thereby improving engine efficiency and performance; therefore, the front auxiliary inlet is regarded as a solution with broad applicability, capable of meeting the requirements of inlet performance under different operating conditions.

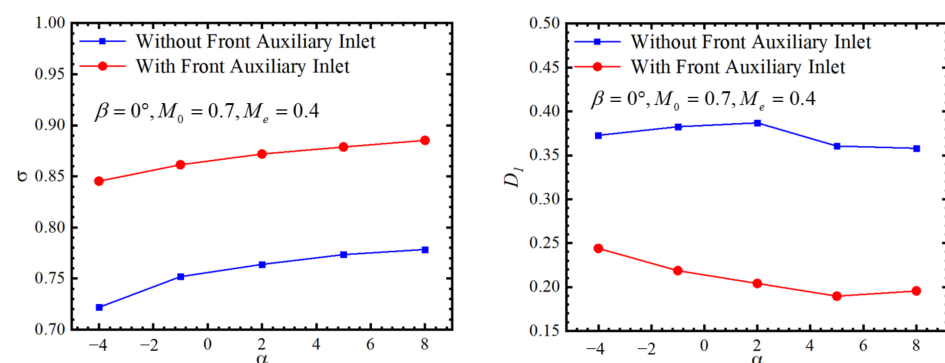


**Figure 19.** Comparison of inlet performance at different angles of attack.

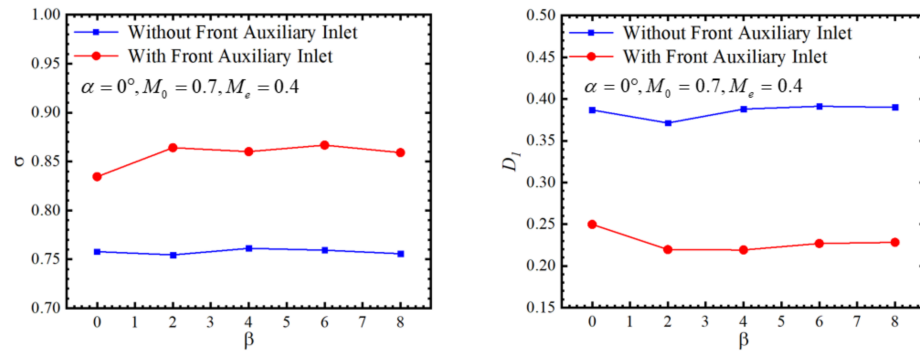


Figure 20. Comparison of inlet performance at different angles of sideslip.

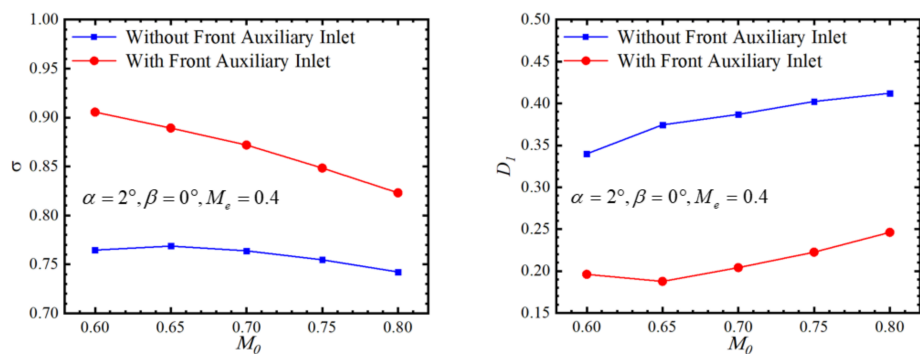


Figure 21. Comparison of inlet performance at different inflow Mach numbers.

### 6. Multi-Parameter Sensitivity Analysis of Front Auxiliary Inlet

The selection of parameters for the front auxiliary inlet has a significant impact on the intake performance. During the design process, it is crucial to determine the extent of the influence of the design parameters on the performance indicators. This can greatly enhance design efficiency and reduce the design cycle. In this section, a standardized dimensionless method is utilized to calculate the sensitivity  $S_i$ , reflecting the influence of the design parameters of the front auxiliary inlet on the characteristic index. Next, the Pareto diagram depicts the proportion of the influence of multiple front auxiliary inlet parameters on the total pressure recovery coefficient and total pressure distortion index at the inlet outlet  $\bar{S}_i$ .

The Pareto diagram serves as a parameter sensitivity analysis tool, displaying the primary factors influencing a particular index. Formulas (3) and (4) exhibit the calculation formulas for  $S_i$  and  $\bar{S}_i$ , respectively. When  $S_i$  is positive, it indicates an overall increase in the indicators with an increase in the local parameters, and the two demonstrate a positive correlation as a whole. Conversely, when  $S_i$  is negative, it suggests an overall index decrease with an increase in the local parameters, and the two reveal a negative correlation as a whole.  $\bar{S}_i$  describes the proportion of the influence of each local parameter on the overall index when multiple local parameters affect a particular overall index. The sum of the impact of each parameter in the same Pareto diagram on the overall index should be 100%.

$$S_i = \frac{\partial f(X)/f(X)}{\partial x_i/x_i} \tag{3}$$

In Formula (3),  $X$  is the value of the local parameters;  $f(X)$  is the value of the overall index when the local parameter takes  $X$ ; and  $x_i$  is the value of the local parameter of item  $i$ .

$$\bar{S}_i = \frac{|S_i|}{\sum_{i=1}^I |S_i|} \tag{4}$$

In (4),  $i$  denotes the local parameter of item  $i$  and  $l$  represents the number of local parameters.

Figure 22 displays the Pareto diagram for the primary parameters of the front auxiliary inlet on intake performance. Orange represents a positive correlation, while green signifies a negative correlation. Among the main parameters of the front auxiliary inlet, the area expansion ratio ( $k$ ) has the most significant impact on the total pressure recovery coefficient and distortion index, accounting for 43.0% and 52.9%, respectively. The second parameter is the front auxiliary inlet opening area ( $S_{front,inlet}$ ), which is responsible for 36.4% and 21.5% of the total pressure recovery coefficient and distortion index, respectively. The third parameter is the centerline offset of the front auxiliary inlet ( $L_2$ ), which accounts for 13.6% and 16.9% of the total pressure recovery coefficient and distortion index, respectively. The distance between the rear lip of the front auxiliary inlet and the front lip of the main inlet ( $L_1$ ) has the least influence on the total pressure recovery coefficient and distortion index, accounting for 7.0% and 8.7%, respectively.

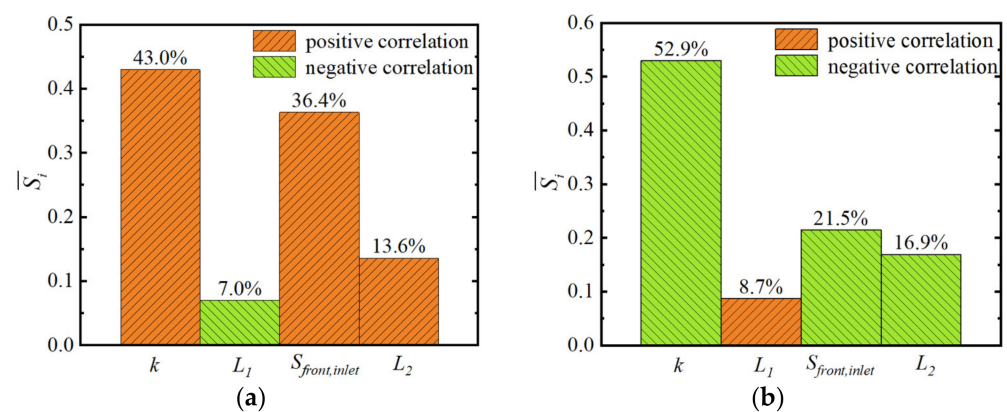


Figure 22. The Pareto diagram of the main parameters of the front auxiliary inlet to the intake performance. (a)  $\sigma$ ; (b)  $D_1$ .

## 7. Conclusions

This article proposes a design scheme for the front auxiliary inlet in order to improve the performance of a submerged intake system, and the main parameters of this scheme were optimized using particle swarm optimization (PSO). Subsequently, a comparative analysis of the flow characteristics of two submerged inlet configurations, one with the front auxiliary inlet and one without, was conducted using computational fluid dynamics (CFD) numerical simulation. To enhance design efficiency and shorten the design cycle, a sensitivity analysis of the key parameters of the front auxiliary inlet was also performed. By analyzing the influence of different parameters on performance, the design direction can be quickly determined, thereby accelerating the design optimization process and improving the design's effectiveness. The following conclusions have been obtained:

- (1) When an electromagnetic shielding grille is installed at the entrance, the performance of the submerged inlet system will significantly decrease. Under the specified design conditions ( $M_0 = 0.7$ ,  $Me = 0.4$ ,  $\alpha = 2^\circ$ ,  $\beta = 0^\circ$ ), the total pressure recovery coefficient is only 0.7638, and the total pressure distortion index is as high as 0.3869. This type of intake performance is unacceptable for the engine. The reason for the decrease in intake performance is that the electromagnetic shielding grille reduces the effective area of the entrance. Furthermore, the installation of the electromagnetic shielding grille prevents the utilization of the pressure gradient in the incoming flow direction and the swirling vortices generated on the sides to drive external airflow into the intake duct. Lastly, when the airflow enters the intake duct through the grille holes, the airflow contracts and its velocity increases; when the airflow exits through the grille holes, the airflow expands and its velocity decreases. This results in "shock

- losses" during the process of flow entering and exiting the grille, further reducing the airflow energy entering the intake duct.
- (2) Under cruise conditions ( $M_0 = 0.7$ ,  $Me = 0.4$ ,  $\alpha = 2^\circ$ ,  $\beta = 0^\circ$ ), the front auxiliary inlet configuration has a total pressure recovery coefficient of 0.8719 and a total pressure distortion index of 0.2041. Compared to the without front auxiliary inlet configuration, the total pressure recovery coefficient increased by 12.39%, and the total pressure distortion index decreased by 47.24%. By observing the development of the boundary layer upstream, the distribution of the total pressure inside the intake duct, the distribution of Mach numbers, and the development of streamwise vortices, it can be seen that the front auxiliary inlet and main inlet forms a device similar to an ejector. The front auxiliary inlet first absorbs low-energy airflow to ensure that the incoming airflow in the main inlet has higher energy. Then, it uses the high-energy airflow in the main inlet to drive the low-energy airflow in the front auxiliary inlet. At the intersection of the front auxiliary inlet and the main inlet, through the mixing action between airflow of different velocities, the high-energy airflow transfers energy to the low-energy airflow. This plays a crucial role in suppressing the development of separation vortices on the side with a larger curvature radius in the inlet; therefore, the design of the front auxiliary inlet can effectively improve the performance of the inlet.
  - (3) Within the calculations conducted in this study, the front auxiliary inlet has been shown to increase the total pressure recovery coefficient and reduce the total pressure distortion index, regardless of variations in the incoming Mach numbers ( $M_0$ ), angle of attack ( $\alpha$ ), and sideslip angle ( $\beta$ ) conditions. Its performance advantage is not limited to specific operating conditions but exhibits broad applicability. It injects additional energy into the intake system and improves the distribution of airflow; therefore, the front auxiliary inlet is a versatile solution with wide applicability, capable of meeting the intake performance requirements under different operating conditions.
  - (4) According to the sensitivity analysis results, the area expansion ratio ( $k$ ) and front auxiliary inlet opening area ( $S_{front,open}$ ) have a significant impact on the intake performance, while the centerline offset of the front auxiliary inlet ( $L_2$ ) and the distance between the rear lip of the front auxiliary inlet and the front lip of the main inlet ( $L_1$ ) have a relatively smaller influence.  $k$  determines the flow conditions inside the front auxiliary inlet. A larger  $k$  reduces the flow velocity and increases the flow pressure, while a smaller  $k$  increases the flow velocity and reduces the flow pressure.  $S_{front,open}$  is closely related to the captured flow rate in the front auxiliary inlet; therefore, when designing the front auxiliary inlet, it is important to focus on and optimize the  $k$  and  $S_{front,open}$ . The  $L_1$  and  $L_2$  have a relatively smaller impact on the performance and can be considered appropriately in the design.

**Author Contributions:** Conceptualization, J.Z. and B.M.; methodology, Zhan, H.; software, J.Z.; validation, J.Z.; formal analysis, J.Z.; investigation, J.Z.; resources, H.Z. and B.M.; data curation, J.Z.; writing—original draft preparation, J.Z.; writing—review and editing, J.Z.; visualization, J.Z.; supervision, H.Z. and B.M.; project administration, B.M.; funding acquisition, H.Z. and B.M. All authors have read and agreed to the published version of the manuscript.

**Funding:** This research was funded by [National Natural Science Foundation of China] grant number [12202363] and [the Natural Science Basic Research Program of Shaanxi] grant number [2021]Q-084].

**Institutional Review Board Statement:** Not applicable.

**Informed Consent Statement:** Not applicable.

**Data Availability Statement:** The relevant information of numerical calculation has been reflected in the manuscript in the form of pictures, charts, etc.

**Conflicts of Interest:** The authors declare no conflict of interest.

## Nomenclature

$\sigma$	Total pressure recovery coefficient
$D_1$	Total pressure distortion index
$\mu$	The ratio of total pressure recovery coefficient to total pressure distortion index
$P$	Mass-averaged total pressure
$P_{AIP}$	Mass-averaged total pressure over the aerodynamic interface plane, Pa
$P_0$	Freestream total pressure, Pa
$P_{AIP,max}$	Maximum total pressure over the aerodynamic interface plane, Pa
$P_{AIP,min}$	Minimum total pressure over the aerodynamic interface plane, Pa
$M$	Mach number
$M_e$	Mach number at the exit
$M_0$	Freestream Mach number
$\alpha$	Angle of attack, °
$\beta$	Angle of sideslip, °
$i$	Grille diversion angle, °
$t$	Grille thickness, mm
$d$	Characteristic size of grille hole, mm
$s$	Adjacent grille hole spacing, mm
$p$	Grille porosity
$\theta$	Front auxiliary inlet diversion angle, °
$S_{front,open}$	Front auxiliary inlet entrance area, mm <sup>2</sup>
$S_{front,throat}$	Front auxiliary inlet throat area, mm <sup>2</sup>
$S_{front,outlet}$	Front auxiliary inlet exit area, mm <sup>2</sup>
$k$	Area expansion ratio
$L_1$	The distance between the rear lip of the front auxiliary inlet and the front lip of the main inlet, mm
$L_2$	Centerline offset of front auxiliary inlet, mm
$n$	The number of grille holes along the flow direction
$0$	Freestream
$e$	Exit
$AIP$	Aerodynamic interface plane
$AIP,max$	Maximum value on the aerodynamic interface plane
$AIP,min$	Minimum value on the aerodynamic interface plane
$front,open$	Front auxiliary inlet entrance
$front,throat$	Front auxiliary inlet throat
$front,outlet$	Front auxiliary inlet exit

## References

- Jia, G.W.; Yin, P.; Shao, S.; Wang, J. Review of RCS measurement and imaging methods of stealth aircraft. *J. Natl. Univ. Def. Technol.* **2022**, *44*, 93–103.
- Zheng, R.S.; Qi, K.N.; Zhang, Q.B.; Xiao, Z.H.; Liu, H.J. Integrated Investigation of Aerodynamic Shape and Stealth Performance for Supersonic Vehicle with “X” Sawtooth Lip Inlet. *J. Propul. Technol.* **2017**, *38*, 2471–2478. [[CrossRef](#)]
- Yu, X.H.; Zhao, Y.M. A Study on Stealth Technology in UAV Inlet Design. *Flight Dyn.* **2007**, *4*, 69–72. [[CrossRef](#)]
- Shi, L.; Guo, R. Electromagnetic Scattering of a Submerged Inlet. *Acta Aeronaut. Astronaut. Sin.* **2008**, *05*, 1098–1104.
- Anderson, B.H.; Reddy, D.R.; Kapoor, K. Study on computing separating flows within a diffusion inlet S-duct. *J. Propuls. Power* **1994**, *10*, 661. [[CrossRef](#)]
- Harloff, G.J.; Smith, C.F.; Bruns, J.E.; Debonis, J.R. Navier-Stokes analysis of three-dimensional S-ducts. *J. Aircr.* **1993**, *30*, 526–533. [[CrossRef](#)]
- Frick, C.W.; Davis, W.F.; Randall, L.M.; Mossman, E.A. *An Experimental Investigation of NACA Submerged Duct Entrances*; Technical Report Archive & Image Library: Washington, DC, USA, 1945.
- Axelson, J.A.; Taylor, R.A. *Preliminary Investigation of the Transonic Characteristics of an NACA Submerged Inlet*; Technical Report Archive & Image Library: Washington, DC, USA, 1950.
- Hall, C.F.; Frank, J.L. *Ram-Recovery Characteristics of NACA Submerged Inlets at High Subsonic Speeds*; Technical Report Archive & Image Library: Washington, DC, USA, 1948.
- Mossman, E.A.; Randall, L.M. *An Experimental Investigation of the Design Variables for NACA Submerged Duct Entrances*; Technical Report Archive & Image Library: Washington, DC, USA, 1948. [[CrossRef](#)]

11. Taylor, R.A. *Some Effects of Side-Wall Modifications on the Drag and Pressure Recovery of an NACA Submerged Inlet at Transonic Speeds*; Technical Report Archive & Image Library: Washington, DC, USA, 1952.
12. Anderson, W.E.; Frazer, A.C. *Investigation of an NACA Submerged Inlet at Mach Numbers from 1.17 to 1.99*; Technical Report Archive & Image Library: Washington, DC, USA, 1952.
13. Sun, S.; Guo, R.R. Experimental Research of Effects of Entrance Parameters on Performance of Submerged Inlet. *Acta Aeronaut. Astronaut. Sin.* **2005**, *26*, 268–275.
14. Xie, W.Z.; Yang, S.Z.; Zeng, C.; GUO, S. Effects of forebody boundary layer on the performance of a submerged inlet. *Aeronaut. J.* **2021**, *125*, 1260–1281. [[CrossRef](#)]
15. Guo, R.W.; Liu, S.Y. Design of submerged inlet. *J. Nanjing Univ. Aeronaut. Astronaut.* **2002**, *33*, 8–12. [[CrossRef](#)]
16. Yang, A.L. An Investigation on Design and Performance for a Submerged Air Intake. *Acta Aerodynam. Sin.* **1998**, *16*, 154. [[CrossRef](#)]
17. Taskinoglu, E.; Knight, D. Design Optimization for Submerged Inlets. In Proceedings of the 41st Aerospace Sciences Meeting and Exhibit, Las Vegas, NV, USA, 24–28 July 2003.
18. Yu, A.Y.; Le, J.L.; Guo, R.W. A study of the design method and an investigation of high speed experiments for a submerged inlet under a stealthy shaped fuselage. *Acta Aerodynam. Sin.* **2007**, *25*, 150–156. [[CrossRef](#)]
19. Wang, Y.G.; Wang, C.H.; Xiao, Y.C.; Chen, B.; Zhou, S.; Guo, J.; Sun, M. Construction methodology for lip surface of a submerged inlet. *Aerosp. Sci. Technol.* **2016**, *54*, 340–352. [[CrossRef](#)]
20. Huang, H.X. Recent Progress in Subsonic S-Shaped Inlets. *J. Propuls. Technol.* **2020**, *41*, 2641. [[CrossRef](#)]
21. Ng, Y.T.; Luo, S.C.; Lim, T.T.; Ho, Q.W. Three Techniques to Control Flow Separation in an S-Shaped Duct. *AIAA J.* **2011**, *49*, 1825–1832. [[CrossRef](#)]
22. Harouni, G.A. Flow control of a boundary layer ingesting serpentine diffuser via blowing and suction. *Aerosp. Sci. Technol.* **2014**, *39*, 472–480. [[CrossRef](#)]
23. Saheby, E.B.; Huang, G.; Qiao, W.; Tang, W. Highly Integrated Inlet Design Based on the Ridge Concept. *J. Propuls. Power* **2016**, *32*, 1–11. [[CrossRef](#)]
24. Huang, G.; Saheby, E.B.; Akhlaghi, M.; Yu, Z. Effects of Ridge Configuration on the Performance of Integrated inlets. In Proceedings of the AIAA/SAE/ASEE Joint Propulsion Conference and Exhibit, Salt Lake City, UT, USA, 25–27 July 2016. [[CrossRef](#)]
25. Delot, A.L.; Scharnhorst, R. Computational and Experimental Results for Flows in a Diffusing S-Duct without and with Flow Control Devices. In Proceedings of the 51st AIAA/SAE/ASEE Joint Propulsion Conference, Orlando, FL, USA, 27–29 July 2015. [[CrossRef](#)]
26. Keerthi, M.C.; Kushari, A. Effectiveness of vortex generator jets and wall suction on separated flows in serpentine-duct diffuser. *Aerosp. Sci. Technol.* **2014**, *34*, 12–19. [[CrossRef](#)]
27. Perez, C.C.; Ferreira, S.B.; Silva, L.F.F.D.; Jesus, A.B.D.; Oliveira, G.L. Computational Study of Submerged Air Inlet Performance Improvement Using Vortex Generators. *J. Aircr.* **2007**, *44*, 1574–1587. [[CrossRef](#)]
28. Ren, S.; Li, X.; Guo, R. Flow field control on the submerged inlet. *Acta Aeronaut. Astronaut. Sin.* **2000**, *21*, 226–229.
29. Huang, G.; Saheby, E.B.; Hays, A. Propulsive Efficiency of Ridge/Inlet Configuration. *Int. J. Aerosp. Eng.* **2018**, *2*, 7462024. [[CrossRef](#)]
30. Jirasek, A. Design of Vortex Generator Flow Control in Inlets. *J. Aircr.* **2006**, *43*, 1886–1892. [[CrossRef](#)]
31. Gissen, A.N.; Vukasinovic, B.; Mcmillan, M.L.; Glezer, A. Distortion Management in a Boundary Layer Ingestion Inlet Diffuser Using Hybrid Flow Control. *J. Propuls. Power* **2014**, *30*, 834–844. [[CrossRef](#)]
32. Saheby, E.B.; Shen, X.; Huang, G.; Anthony, P.H. Flow structure of the ridge integrated submerged inlet. *Aerosp. Sci. Technol.* **2021**, *119*, 107136. [[CrossRef](#)]
33. Sun, S.; Tan, H.J.; Wang, C.X. Submerged Inlet Performance Enhancement Using a Unique Bump-Shaped Vortex Generator. *J. Propuls. Power* **2016**, *32*, 1275–1280. [[CrossRef](#)]
34. Guo, S.W. Numerical Analysis and Experimental Validation of a Submerged Inlet on the Plane Surface. *Chin. J. Aeronaut.* **2005**, *18*, 199–205. [[CrossRef](#)]
35. Harrison, N.A.; Anderson, J.; Fleming, J.L.; Ng, W.F. Active Flow Control of a Boundary Layer-Ingesting Serpentine Inlet Diffuser. *J. Aircr.* **2013**, *50*, 262–271. [[CrossRef](#)]
36. Yadav, K.R.; Paul, A.R.; Hegde, N.; Jain, A. A Comparison of Circular and Slotted Synthetic Jets for Flow Control in a Twin Air Intake. *Def. Sci. J.* **2020**, *70*, 113–121. [[CrossRef](#)]
37. Cheng, D.S.; Sun, S.; Wen, Y.F.; Tan, H.J. Submerged inlet performance improvement with blowing on fuselage. *J. Aerosp. Power* **2012**, *27*, 1131–1138.
38. Cheng, D.S.; Tan, H.J.; Sun, S.; Tong, Y. Computational Study of a High-Performance Submerged Inlet with Bleeding Vortex. *J. Aircr.* **2012**, *49*, 852–860. [[CrossRef](#)]
39. Rein, M.; Koch, S. Experimental Study of Boundary-Layer Ingestion into a Diverterless S-Duct Intake. *AIAA J.* **2015**, *53*, 3487–3492. [[CrossRef](#)]

**Disclaimer/Publisher’s Note:** The statements, opinions and data contained in all publications are solely those of the individual author(s) and contributor(s) and not of MDPI and/or the editor(s). MDPI and/or the editor(s) disclaim responsibility for any injury to people or property resulting from any ideas, methods, instructions or products referred to in the content.